Materials Advances

ROYAL SOCIETY OF CHEMISTRY

PAPER

View Article Online
View Journal | View Issue

Cite this: *Mater. Adv.*, 2026, 7, 2641

Microfluidic-mixer assisted 3D printing of functionally graded multimaterial hydrogels for engineering complex tissue interfaces

Maria Celeste Tirelli, [a] Francesco Nalin, [a] Nehar Celikkin, [a] Żaneta Górecka, [a] Pasquale Posabella, [b] Wojciech Święszkowski [b] and Marco Costantini *[a]

Received 2nd October 2025,
Accepted 21st January 2026

DOI: 10.1039/d5ma01130b

rsc.li/materials-advances

Reconstructing complex tissue interfaces, such as the osteochondral junction, requires biomaterials capable of mimicking the native gradients in mechanical, biochemical, and structural properties. Traditional fabrication methods often are not able to achieve continuous and tunable transitions within a single construct. To overcome these limitations, we developed a novel microfluidic-assisted 3D printing platform where a high-efficiency passive micromixer with a flow-focusing junction (mix-ff-MPH) was used as a printhead. This technique enables the manufacturing of functionally graded porous hydrogels (FGPHs) with smooth gradients by real-time control of polymer composition and density during extrusion. By optimizing micromixer geometries, we achieved high mixing efficiency (mixing index $\geq$0.8), ensuring uniform integration of distinct bioinks such as gelatin methacrylate (GelMA) and dextran methacrylate (DexMA). The resulting constructs exhibit spatially controlled gradients in porosity and composition, confirmed by confocal microscopy and FTIR spectroscopy. When seeded with 3T3 fibroblasts, the scaffolds demonstrated region-specific cell adhesion and proliferation, highlighting the role of locally defined porosity and composition in guiding cellular behavior. This platform provides a versatile and precise method for fabricating graded hydrogels and holds significant promise for applications in tissue engineering, especially in addressing the long-standing challenge of replicating the intricate organization of native tissue interfaces.

1. Introduction

All multicellular biological organisms, regardless of class, family, or species, share one significant characteristic: heterogeneity. This intrinsic heterogeneity is the result of a refined hierarchical organization, which extends from the macro ($\sim 10^{-1}$ m) down to the molecular ($\sim 10^{-9}$ m) scale. The latter feature is even more pronounced at interface regions where the structural organization of one tissue smoothly transit or is connected to a different one. These transitional zones introduce an additional layer of complexity, as their physical, chemical and biological properties are precisely spatially patterned to create unique gradients.[1] A notable example of such intricacy lies in the osteochondral interface. This specialized interface exhibits a specific architecture, transitioning from the highly dense, soft cartilage region to the subchondral bone, stiff framework of the bone, with variations in matrix composition, microarchitecture, and cellular heterogeneity.[2]

The key challenge in engineering tissue interfaces (TI) is replicating the multiscale hierarchical structure.[3] To address this, TI scaffolds must be designed to mimic the mechanical properties, internal microarchitecture, and organization of natural tissues.[4,5] These biomimicking complex gradients in composition and porosity can be achieved by leveraging functionally graded porous hydrogels (FGPHs). Recent innovations have introduced FGPHs as a cutting-edge approach in tissue engineering, expanding the potential for creating scaffolds with tailored gradients in composition and porosity.[6] FGPHs specifically designed for tissue interfaces are commonly manufactured using freeze-drying,[7] solvent casting,[8] and 3D printing[9] to achieve tunable mechanical properties and well-defined density gradients. However, these approaches are limited to controlling overall architecture and mechanics, and do not allow precise, spatially tunable porosity at the microscale, which is critical for replicating the hierarchical structures of tissue interfaces.[2] Microfluidic devices generating monodisperse emulsions and creating customized templates have emerged as a prominent technique for fabricating FGPHs with controlled porosity and mechanical properties.[10] Droplet generation techniques as step-emulsification,[11] T-junction,[12] and flow-focusing[10,13] enable the precise production of bubble or droplet patterns,

[a] *Institute of Physical Chemistry – Polish Academy of Science, Warsaw, Poland. E-mail: mcostantini@ichf.edu.pl*
[b] *Faculty of Materials Science and Engineering, Warsaw University of Technology, Warsaw, Poland*

allowing the formation of FGPHs with a controlled internal architecture. Despite enabling significant achievements in controlling inner architecture, these systems are still in their infancy when it comes to creating multi-material biomaterial inks, a key requirement for tissue interfaces. Currently, multi-inlet microfluidic setups designed to generate composition gradients mostly produce Janus fibers rather than creating a uniform multi-material matrix composition.[14] Microfluidic micromixers have been identified as a refined approach to replicate the smooth compositional transition found at the tissue interface.[15] They enables precise modulation and mixing of different solutions inks,[16] producing a broad palette of new material compositions. If integrated with the flow-focusing junction, this novel microfluidic device could offer a promising strategy for an extrusion system capable of precisely controlling both internal architecture and material composition.,[17–19] generating FGPHs with seamless and gradual transitions in architectural, mechanical, and biochemical properties, potentially recapitulating the complexity of the native tissue interface.[1] Here, we present a microfluidic-enhanced 3D printing approach that enables controlled fabrication of graded biomaterials, with potential for recreating complex tissue-like structures. We introduce a novel microfluidic printing head (mix-ff-MPH) with an integrated passive micromixer for 3D printing porous, chemically graded hydrogels with precise spatial control. The system enables dynamic tuning of scaffold porosity and composition, leading to localized cellular responses based on material properties. Preliminary tests show that scaffold regions enriched with different biomaterials influenced fibroblast behaviour, highlighting the tool's potential for advanced tissue engineering and biofabrication applications.

2. Materials and methods

2.1. Materials

Dextran from Leuconostoc spp., $M_r \approx 70\,000$), gelatin (from porcine skin, 300 bloom, Type A), DMSO, glycidyl methacrylate (GMA), methacrylic anhydride, hexadecane (99%), plantacare, 2-hydroxy-4′-(2-ydroxyethoxy)-2-methylpropiophenone (Irgacure 2959), hydrochloric acid (HCl), tin chloride (SnCl2), phosphate-buffered saline (PBS), 4-dimethylaminopyridine (DMAP, 99%), Calbiochem™ OmniPur™ Agarose. All chemicals were purchased from Sigma-Aldrich and used without further purification unless otherwise stated.

2.2. Synthesis of dextran-methacryloyl

DexMA was synthesized following an established protocol, that was already published.[10] Briefly, a round bottom flask was used to dissolve dextran (10 g) in DMSO (90 mL). Then, DMAP (2 g) was dissolved in DMSO, followed by the addition of a specific amount of GMA (4 mL, equivalent to 50% of the moles of dextran repeating units). The reactants were stirred gently (100 RPM) and left to react in the dark at room temperature for 48 hours. The reaction was stopped by adding an equimolar volume of HCl to neutralize the DMAP. The solution was dialyzed (dialysis tube molecular weight cut-off = 1 kDa) for 5 days against deionized water until the water achieved its nominal conductivity of 18 MΩ cm. Dialyzed DexMA solution was freeze-dried and stored at 4 °C until further use.

2.3. Synthesis of gelatin-methacryloyl

GelMA was synthesized using a previously documented protocol.[10] Gelatin was dissolved at 10% w/v in PBS (pH 7.4) at 50 °C. Under constant vigorous stirring (500 RPM), methacrylic anhydride (0.8 mL per gram of gelatin) was added to the gelatin solution, and the mixture was left to react for 3 hours. GelMA solution was dialyzed against deionized water at 50 °C using 14 kDa cut-off dialysis tubes until the water achieved its nominal conductivity of 18 MΩ cm. Dialyzed GelMA solution was freeze-dried and stored at 4 °C until further use.

2.4. Preparation of 3D printing supporting bath

The supporting bath was prepared according to the standard operating protocol.[20] Briefly, 0.5 g of agarose was dispersed in 100 mL of deionized water and the suspension was autoclaved at 121 °C for 20 minutes. Later, the agarose solution was removed from the autoclave and cooled down to room temperature under continuous stirring at 700 RPM for 12 hours. The fluid–gel agarose was kept at room temperature until further use.

2.5. Fabrication of polycarbonate microfluidic chip

Polycarbonate sheets were used to create the micromixer-flow-focusing microfluidic chip with the following characteristics: continuous and dispersed phase inlet 250 μm, mixer channel = 400 μm; mixer repetitive unit 5 mm; orifice width = 100 μm; output channel width = 500 μm; channels depth = 200 μm; printing nozzle coupled to the outlet channel = 25 G. The microfluidic chips were fabricated using a procedure reported previously.[21] Briefly, a CNC milling machine (MSG402, ErgWind, Poland) was used to engrave 5 mm thick polycarbonate sheets. The sheets were then sonicated in isopropanol for 30 minutes before being sealed in a hot press at 130 °C for 30 minutes. Afterward, the microchannels were modified with 20% $SnCl_2$ in ethanol (w/v). The channels were flushed for 2 h at a continuous flow rate of 20 mL h^{-1} at 60 °C to prevent the interaction between polycarbonate and organic inner phase.[22] Finally, the microchannels were rinsed with deionized water to remove excess $SnCl_2$.

2.6. Rheological measurement

Rheological properties of the continuous phase solutions (DexMA + Plantacare and GelMA + DexMA + Plantacare) were analyzed using a rotational rheometer (Malvern Kinexus Pro) at 35 °C equipped with a cone-plate geometry. This temperature was selected to prevent thermal gelation of GelMA while simulating printing conditions. The shear behavior of the samples was assessed by applying a shear rate from 1 to 10^3 Hz.

2.7. Microfluidic mixing and emulsion generation

The organic and aqueous phases were filtered using a 0.2 μm pore syringe filter to avoid clogging the microchannels before starting each experiment. The micromixer was used to passively

mix the two aqueous biomaterial inks (20% DexMA + 1% Plantacare + 1% Irgacure 2959 and 10% GelMA + 2%DexMA + 1% Plantacare + 1% Irgacure 2959). The mixed aqueous solution was then used as a continuous phase to produce an oil-in-water emulsion using a flow-focusing junction, with hexadecane as the dispersed phase. The mixing of the continuous phases and the droplet generation was precisely controlled by varying the flow rates of the different phases using microfluidic pumps (neMESYS, Cetoni GmbH). All porous materials were printed with a dispersed phase volume fraction (φ_D) in the range of 0.2–0.8, and the total flow rate of the two phases was adjusted to 20 μL min^{-1}. The generation of the emulsion and the mixing of the two different solutions was observed with a high-speed camera (IDS, Germany) at 165 fps at a magnification of 1×.

2.8. Mixing index

The mixing index (MI) serves as a quantitative parameter to evaluate the performance of a microfluidic mixer. In view of its application in 3D printing of scaffold for cell seeding, the mixing performance of five different microfluidic printhead (MPH) (Fig. 1a) (Fig. S1) were tested using two solutions showing different viscosities at 35 °C (Fig. 1). The MI was estimated based on image analysis of a cross-sectional plane perpendicular to the flow direction and is defined as:

$$\mathrm{MI} = 1 - \frac{\sqrt{\frac{1}{N}\sum_{i=1}^{N}(C_i - \bar{C})^2}}{\bar{C}} \quad (1)$$

where N is the number of sampling points in a chosen cross-section, C_i is the point concentration (calculated from pixel intensity) of the analyzed specimen, and C is its mean concentration along the cross-section.

The experiment for the evaluation of MI were conducted by introducing the DexMA and GelMA solutions through their respective inlets of the micromixer, maintaining a constant combined flow rate of 14 μL min^{-1} to replicate the conditions of the 3D printing process. To assess how different feeding rates influence the Mixing Index (MI) with various micromixer architectures, the ratio GelMA:DexMA solutions supplied to the MPH for each analysis were adjusted for 100 : 0, 80 : 20, 50 : 50, 20 : 80, and 0 : 100. For example, in the 80 : 20 ratio condition, flow rates of 11.2 μL min^{-1} for GelMA and 2.8 μL min^{-1} for dextran were utilized (Table S1). For imaging purposes and to distinguish between the two colorless biomaterial inks, DexMA was labeled with rhodamine and GelMA with FITC. Subsequently, laser confocal images were captured and processed to calculate the MI.

2.9. Emulsion 3D printing of cubic porous scaffold and complex geometries

A custom-made 3D printer was employed for the fabrication of the FGPSs, with the neMESYS software managing the operation of three microfluidic pumps (neMESYS, Cetoni GmbH) connected to the 3D printing system. The deposition of emulsion fibers in 3D was accomplished through a linear axis system arranged in a Cartesian configuration driven by a stepper motor. Printing was performed in a temperature-controlled chamber at 35 °C to ensure stable processing conditions. To standardize the 3D printing process and conduct a comparative analysis of gradient emulsion printing, 3D cubes were printed in an agarose fluid–gel bath. The 3D structure that resulted impossible to be printed in air, with an over-hang $>45^{\circ}$, was printed with porous fibers in agarose fluid–gel with a print speed of 3.3 mm s^{-1} (F200). The complex geometries and cubes were designed in Inventor's CAD program (Autodesk). Subsequently, these models were then sliced with a thickness of 0.3 mm using the STL to G-code conversion application Slic3r. To automate the creation of different porosities inside the same geometry and distinct degrees of mixing for the continuous phases, a Script function code was developed using neMESYS software. The code precisely controlled the microfluidic pumps according to the required flow rates, thereby automating the formation of volume fractions for the dispersed phase. For visualization of gradients in the printed geometries, fluorescent dye was incorporated into the hydrogel solutions.

2.10. Scaffold cross-linking and purification

Irgacure 2959 was utilized as a radical photoinitiator in the external phase to enhance crosslinking of the methacrylated biopolymer chains (DexMA and GelMA). The 3D printing was conducted by avoiding direct light to prevent the radical initiators from premature cross-linking. The printed FGPSs were cross-linked using a UV lamp (λ = 365 nm) for 10 minutes after the emulsions were printed in the agarose supporting solution. The crosslinked constructs were then collected from the agarose fluid–gel with a spatula and the internal organic phase (hexadecane) was eliminated by immersing them in a DMSO solution. The scaffolds underwent multiple washes with DMSO over three days, followed by rinsing with distilled water until nominal conductivity was achieved.

2.11. Spectroscopic analysis

Fourier transform infrared (FTIR) spectra of the DexMA-GelMA gradient samples were recorded using a Nicolet 8700 spectrometer equipped with an attenuated total reflectance (ATR) accessory (Thermo Fisher Scientific, USA). FTIR analysis, based on changes in the vibrational energy of molecular grafts, enables the identification of functional groups and molecular structures. This qualitative technique correlates specific wavenumber regions with characteristic chemical bonds. To obtain each spectrum, scans were acquired in the 400–4000 cm^{-1} range, with a resolution of 4 cm^{-1}. Single-material and gradient scaffolds were 3D-printed, crosslinked, and freeze-dried prior to analysis using an FTIR instrument. Slice (approximately 2 × 2 mm) were manually dissected from predefined positions along the z-axis of the 3D printed gradient scaffolds before FTIR acquisition.

2.12. Mechanical testing of 3D printed scaffolds

The scaffolds' material properties were evaluated *via* mechanical compression tests using a dynamic mechanical analyzer

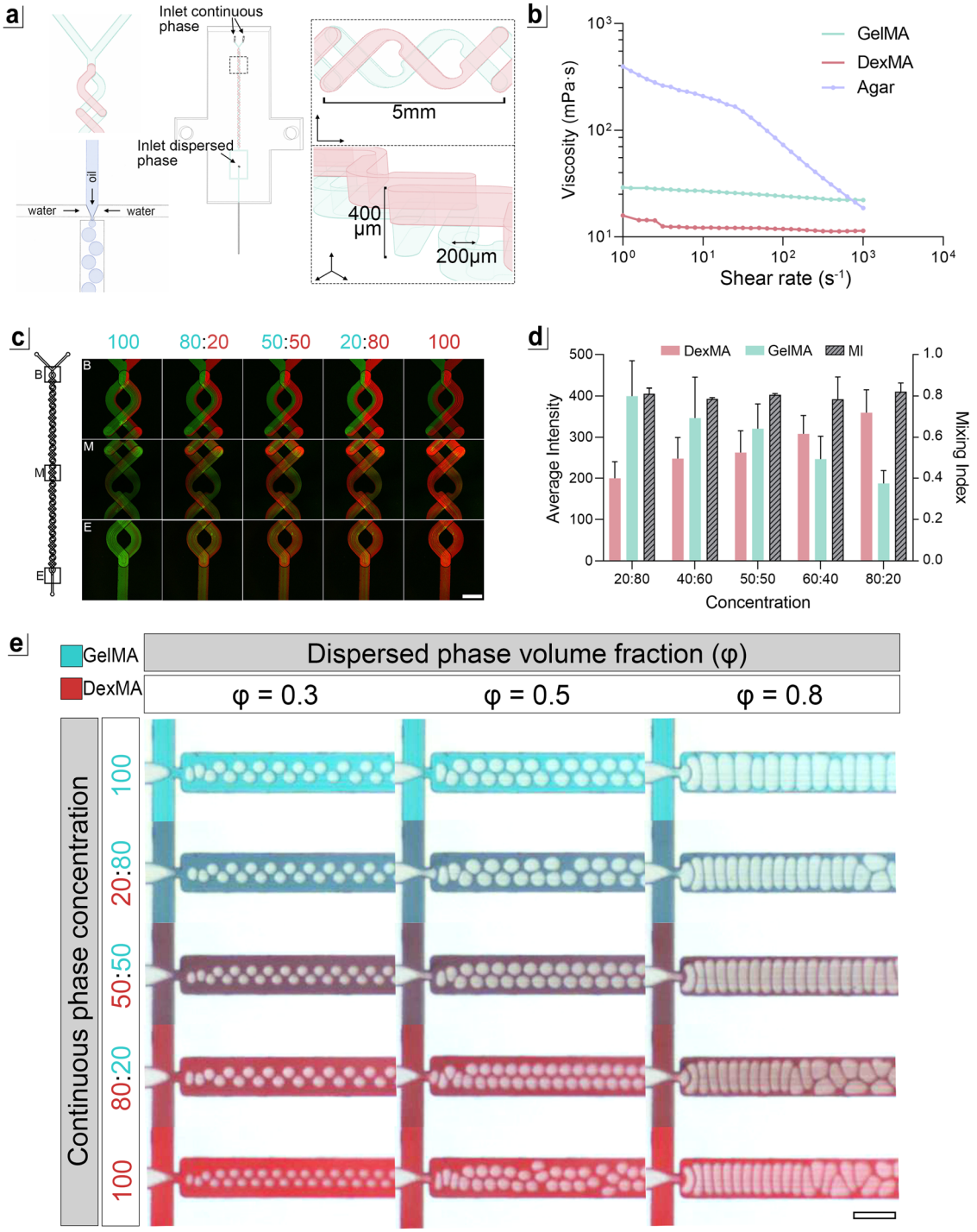

Fig. 1 The microfluidic printhead (mix-ff-MPH) bearing a passive micromixer. (a) Schematic representation of the flow-focusing microfluidic chip (C2) with relative cross sections; (b) rheological characterization of the agarose fluid–gel, DexMA, and GelMA solutions; (c) confocal images of different points of the micromixer beginning (B), middle (M) and end (E) captured at different mixing ratio DexMA (red):GelMA (green); (d) analysis of MI (gray column) and average intensity (green and red column); (e) microfluidic production of the emulsions at various volume fractions of the dispersed phase ($0.2 < \varphi < 0.8$) and at various ratios between two different polymeric solutions DexMA (red) and GelMA (green). Scale bar (c) 800 µm, (e) 500 µm.

(DMA Q800, TA Instruments, New Castle, DE, United States). A static force of 0.001 N was applied before testing. The tests were conducted at room temperature using a ramp strain with a strain rate of 5% min^{-1} until 30% compression. The tested samples had cylindrical dimensions with base diameter of 7 mm, while samples height was automatically detected by the software. Samples were selected to have either single (GelMA or DexMA) or bi-composite material formulation with defined ratios of the two components (DexMA : GelMA = 80 : 20, 60 : 40, 40 : 60). The Young's modulus of each sample was

identified as the slope of the linear elastic part of the stress–strain curve, in the range of 3–5% strain.

2.13. Culture of 3T3-fibroblast and cytocompatibility testing

3T3-fibroblast were cultured in basal DMEM medium supplemented with 10% FBS, 1% P/S, and 1% 1 M HEPES. Before the seeding, cells were detached using trypsin with 0,25% EDTA, centrifuged at 300 × *g* for 5 minutes at room temperature (RT), and suspended in growth media at a concentration of 10^6 cells per mL. Each scaffold was inserted into a 1.5 mL sterile tube and completely submerged with 500 μL cell suspension, resulting in a final seeding of 5×10^5 cells per scaffold (7 × 7 × 2 mm). Then, the tubes with samples were placed on a rotating stage for 1 h in the incubator for homogeneous cell distribution and seeding. Finally, scaffolds were moved to a 24-well plate and cultured under standard conditions (37 °C, 5% CO_2). The medium was completely changed every 2 days.

2.14. Live/dead assay

The viability of 3T3-fibroblasts was evaluated using Live/dead Cell Imaging kit 488/570 (Invitrogen) after 1 and 7 days of cell culture. At the desired time points, following the manufacturer's protocol, the cell-seeded 3D printed constructs were stained with live/dead assay solution and incubated for 15 min at RT. Subsequently, the image acquisition was performed using a confocal microscope (Nikon, A1R), using 488 nm and 561 nm laser sets to detect living and dead cells, respectively. The images were acquired with 10× magnification and the Grab Large Image option to obtain an overview of the entire scaffold.

2.15. Immunofluorescence (IF) staining

3D printed scaffolds seeded with 3T3 fibroblasts were fixed using 4% v/v paraformaldehyde in PBS overnight at RT. The cells were permeabilized with 0.2% v/v Triton X-100 in PBS for 30 minutes at RT, followed by blocking of non-specific binding with 1% (v/v) BSA in PBS for 2 hours at 4 °C. The scaffolds were stained to evaluate the cell attachment and collagen I deposition. Actin filaments were labeled with Alexa Fluor 488-conjugated Phalloidin (Sigma, Germany) (1 : 40 v/v in 1% BSA solution) for 2 hours at RT. For collagen I staining, samples were incubated overnight at 4 °C with a primary anti-collagen I antibody (Sigma, Germany, rabbit-derived) (1 : 100 v/v in 1% BSA solution). After two washes in PBS (5 minutes each), samples were incubated with a Texas Red-conjugated anti-rabbit secondary antibody (1 : 150 v/v in 1% BSA solution) for 2 hours at RT. Finally, nuclei were counterstained with DAPI (Invitrogen) (1 : 1000 in 1% BSA solution) for 10 minutes at RT. IF images were acquired using a Nikon A1R confocal microscope, while image analysis was performed using ImageJ software (National Institutes of Health, USA).

2.16. Cell density determination

Cell density within the scaffolds at different time points was calculated by evaluation of the confocal pictures, utilizing ImageJ Particle analyzer. Areas of 638 × 638 μm^2 were analyzed with respect to the stack height. Resulting cell numbers were divided by the observed analyzed scaffold volume.

2.17. X-ray computed tomography analysis

Morphological analysis of 3D-printed samples was performed *via* X-ray computed tomography (CT), using Skyscan 1172 (Bruker, USA) with a scanning voltage of 40 kV, power of 10 W, and a rotation step of 0.50° over an angle range of 192.50°. Image smoothing and noise reduction were performed *via* NRecon software (Bruker, USA). Data analysis and 3D reconstruction of the models were performed with ImageJ software (National Institutes of Health, USA).

2.18. Statistical analysis

In order to do the statistical analysis, GraphPad Prism (Graph Pad Software Inc., La Jolla, CA) was used. Either one-way ANOVA or two-way ANOVA were used to determine the differences between groups. Significantly different data were identified as $p < 0.05$.

3. Result and discussion

3.1. Micromixer and flow-focusing microfluidic printhead

Recent advancements have demonstrated that microfluidic-assisted 3D printing enables to pattern unique templates for the synthesis of porous hydrogels.[11,13] Moreover, these platforms allows to rapidly switch between different inks in a continuous manner, resulting in heterogenous structures with alternated or co-extruded spatial bioink patterns.[10,11,23] However, the systems proposed so far do not allow to create smooth spatial gradients of the extruded inks, which could be highly beneficial to better recapitulate the matrix and cell graded complexity of native tissue interfaces.[14]

To address this challenge, we developed a novel microfluidic printhead—referred to as mix-ff-MPH—which integrates a passive micromixer upstream of a flow-focusing junction (Fig. 1a). This design enables the precise fabrication of functionally graded porous hydrogels by allowing fine-tuned control over: (i) the chemical composition of the matrix, and (ii) the density and local porous architecture, in either a continuous or discontinuous fashion. The mix-ff-MPH was designed to bear two distinct inlet channels for the supply of the continuous phases converging to a passive serpentine-shaped mixing unit, and one inlet for the dispersed phase of the flow-focusing junction. The operational range of the flow-focusing was settled based on the data obtained in a recent work from our research group.[10] We used as continuous phase Dextran methacrylate (DexMA) or Gelatin methacrylate (GelMA) supplemented with Plantacare as surfactant. As dispersed phase, we used Hexadecane. The total flow rate of the emulsion ink was set at 20 μL min^{-1} as it was found to offer a steady overall emulsion production rate. By keeping the emulsion ink flow rate constant and only adjusting the ratio between the flow rates of the two immiscible phases, one can achieve a volume fraction of the dispersed phase

between 0.2 and 0.8, resulting in droplet size range between 100–400 μm.[10]

To promote the formation and mixing of bioink streamlines, we designed and tested five micromixers (Fig. 1a) (Fig. S1) with different channel geometries that constrain the flow to follow a helical path. As reported in previous studies,[17] certain passive micromixers rely on geometric structures to stretch and fold fluids to enhance molecular diffusion and chaotic advection. The overall mixer geometry, which generally includes obstacles or barriers, as well as a varying number of repeating units, greatly influences the mixing efficiency.[24,25] Selecting an efficient geometry allows for a reduction in mixer length, a crucial parameter in printhead design, as a smaller mixer size would result in a decrease of dead time and volume, improving the synchronization between material gradient generation and extrusion.[11]

The five micromixers feature a two-layer design based on a split-and-recombine structure. Versions A1, A2, and B (Fig. S1) consist of two serpentine channels with forced helixes varying in the length and geometry of the repeating unit. Versions C1 (Fig. S1) and C2 (Fig. 1a) incorporate additional obstacles and barriers into the split-and-recombine structure. The combination of serpentine forced helix channels and obstacles was designed to split and shuffle the streamlines and promote the contact and diffusion of the two bioink solutions, thereby enhancing mixing.

We initially tested the mixing performance of each micromixer using two different solutions, containing DexMA (20% w/v) and GelMA (10% w/v), respectively, tagged with different fluorescent dyes (DexMA-TRITC and GelMA-FITC). The two solutions exhibit a quasi-Newtonian behavior with viscosities in the range of 10^1–10^3 mPa at 35 °C (Fig. 1b). The rheological study was performed at 35 °C to investigate the rheological behavior at the operating temperature and prevent the GelMA solution from undergoing thermal gelation.[26] The solutions were supplied to the mix-ff-MPH, and fluorescence images were taken with a confocal microscope to analyze the mixing index (MI). We conducted the analysis at a constant flow rate of 14 μL min^{-1} which represented the maximum flow rate of the continuous phase used experimentally for 3D printing. Additional MI measurements, collected at 7, 21, and 28 μL min^{-1} for the selected mixer geometry, are provided in the SI (Fig. S2), demonstrating consistent mixing performance across a broader flow-rate range. To investigate the MI at various ink proportions, we used five different GelMA : DexMA volumetric ratios: 100 : 0, 80 : 20, 50 : 50, 20 : 80, and 0 : 100 (Fig. 1c). The obtained results showed that the mixer geometry had a significant impact on the MI, with values ranging from 0.7 to 0.8. We selected for our printing experiments the C2 mixer geometry as it showed an MI $\geq$ 0.8 for all the tested volumetric ratios of GelMA and DexMA inks (Fig. 1d and Fig. S1 SI).[17] A previous study conducted by our research group,[27] employed a simple serpentine mixer with alginate-based inks, achieving a MI $\leq$ 0.6, at least 20% lower than the values obtained in the current work. Such an improvement results from the combined influence of a more complex mixer geometry and the lower viscosity of the solutions used in this study. These findings are in line with the guidelines proposed in a recent review article of different passive micromixer[28] where it was highlighted the necessity of designing passive mixers based on the specific properties of the fluids involved, as both mixer geometry and fluid viscosity are crucial factors influencing mixing performance.

Following the characterization of the passive mixer unit, we explored the feasibility of generating an O/W emulsion with a flow-focusing junction placed downstream of the mixer. As reported in Fig. 1e, the flow-focusing junction was used to generate monodisperse emulsions having volume fractions of the dispersed phase in the range of 0.2 and 0.8. The upstream presence of the micromixer further enabled the modulation of the external phase composition on demand, as indicated by the color-graded switch between red and green. This capability highlights the effectiveness of the mix-ff-MPH in not only ensuring thorough mixing but also enabling precise control over the emulsion's composition.

3.2. 3D printing

The ability to precisely modulate matrix composition and density significantly expands the manufacturing potential of porous functionally graded hydrogels (pFGHs), enabling the creation of materials with finely tuned physicochemical properties. This capability is especially valuable for customizing key characteristics of soft biomaterials—such as mechanical strength, swelling behavior, and cell adhesion—to meet specific biomedical requirements. Moreover, it is expected to have a significant impact for the recapitulation of physiological matrix and cellular gradients typical of native tissues, thus enabling the biofabrication of advanced *in vitro* models of tissue interfaces.

To address this challenge, we equipped a customized 3D printer with the mix-ff-MPH and assessed its capacity in fabricating porous graded hydrogels (Fig. 2a). The printer was placed in a temperature-controlled chamber, and all printing was carried out at 35 °C. By precisely coordinating the flow of the continuous and dispersed phases with the 3D motion of the mix-ff-MPH, we fabricated functionally graded hydrogels (FGHs) with locally tunable porosity and chemical composition. Printing was performed within an agarose fluid–gel bath, which acted as a supportive medium throughout the process. This technique effectively overcomes the challenges of printing complex structures with soft materials such as hydrogels—particularly when using inks (including emulsions) that lack the viscoelasticity required for traditional extrusion-based methods.[20]

A simple two-layer grid composed of TRITC-DexMA and FITC-GelMA was printed to evaluate the ability of the mix-ff-MPH system to precisely control local polymer composition during emulsion fiber deposition. Fluorescence imaging allowed us to visualize spatial variations in polymer composition within the deposited fibers, corresponding to the programmed mixing ratios in the continuous phase. The resulting patterns confirmed that the micromixer enables reliable and tunable blending of the two polymer solutions, producing fibers with the desired local composition (Fig. 2b). To further explore the system's potential for fabricating graded FGHs in three dimensions, we designed and printed 3D cubes ($7 \times 7 \times 7$ mm^3). Fourier-transform infrared (FTIR) spectroscopy

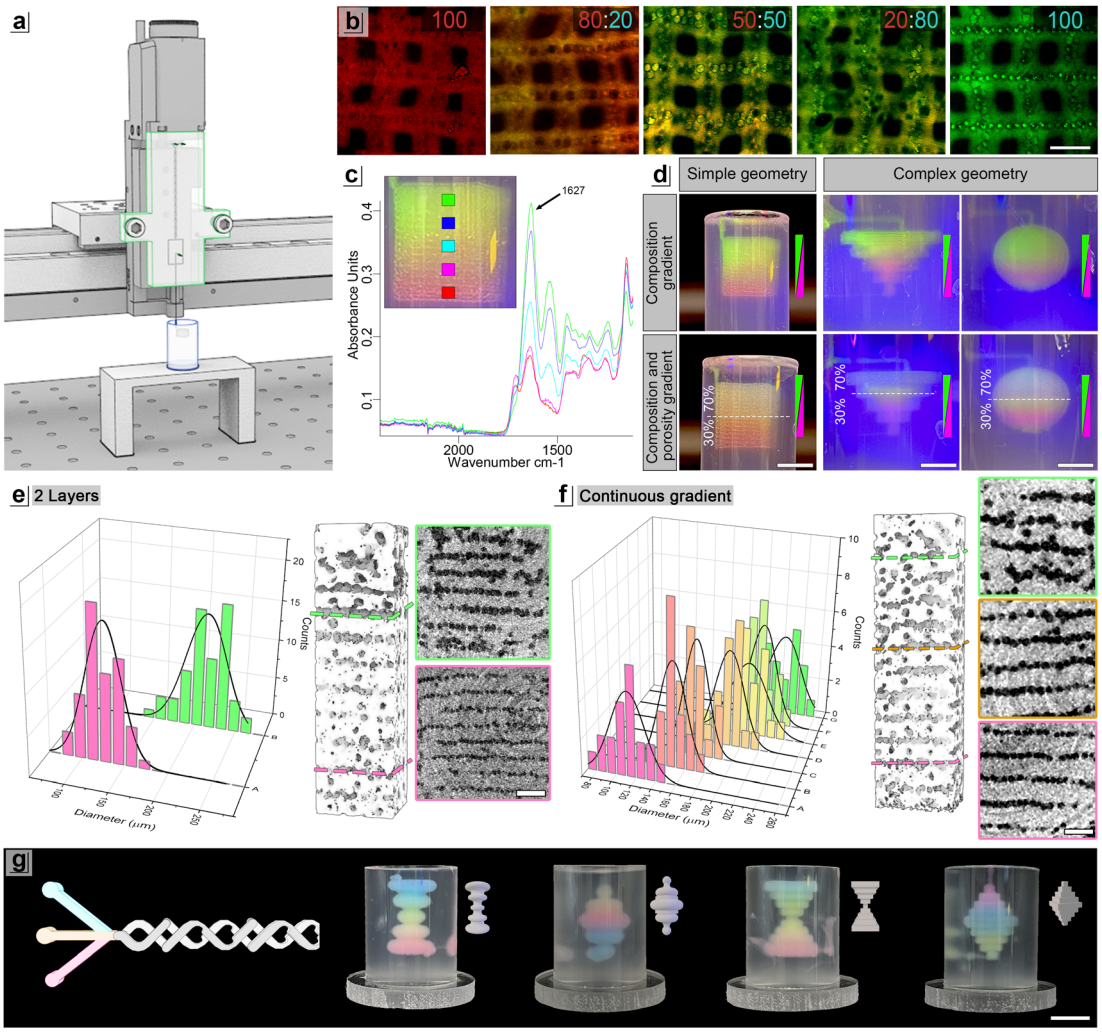

Fig. 2 Operational set-up - (a) schematic representation of 3D printer with the mix-ff chip as printhead; (b) confocal images of 3D printed grids of mixed compositions of DexMA : GelMA at various mixing ratios: 100 : 0,80 : 20, 50 : 50, 20 : 80,0 : 100, reporting the efficiency of the mixing; (c) FTIR spectra at specific points of DexMA:GelMA gradient samples; (d) 3D printed porous structures inside the agarose fluid–gel bath that were printed using two different fluorescent dyes in the continuous phases (the first line exhibits a graded transition between two colors, indicating a compositional gradient between two materials along the *z*-axis. In the second line, while the compositional gradient remains consistent with the first line, a density gradient is introduced. This density variation is evident in the fluorescence intensity of the dyes: regions with a stronger fluorescence signal correspond to higher density (low porosity), whereas regions with a weaker fluorescence signal indicate lower density (high porosity)); (e) and (f) Micro-CT analysis of porous FGMs. Three-dimensional reconstruction of the scaffold obtained from X-ray image stacks and a representative horizontal cross-section (right), together with the corresponding pore size distribution (left). (g) Schematic representation of 3 inlets micromixer and 3D printed complex geometries with gradient composition evidenced by smooth gradient of color. Scale bars: (b) 1 mm, (d) 5 mm (e) 1 mm (f) 500 µm (g) 1 mm.

was conducted at multiple locations along the 3D-printed gradient sample (Fig. S3) to assess the mixing ability of the system. We specifically analysed the amide I band of gelatin at approximately 1627 cm^{-1}, which is primarily associated with C=O stretching vibrations of the peptide backbone (Fig. 2c), The progressive spectral changes observed along the scaffold height align with variations in polymer concentration, confirming that the printed scaffold exhibits a smooth compositional gradient and demonstrating effective polymer mixing along the *z*-dimension.

In addition to the compositional gradient, the developed system is capable of generating simultaneously density gradient within the same printed hydrogels. To demonstrate this, we designed and printed 3D geometries, including both simple shapes, such as cubes, and more complex architectures with overhanging angles exceeding 45° (Fig. 2d). Our results showed that the architectural complexity did not hinder the simultaneous control of local porosity and compositional gradients during the printing process. The fluorescently labelled continuous phase solutions provided immediate visual feedback on the porosity distribution, with higher fluorescence signals indicating regions of lower porosity. The colour intensity differences in Fig. 2d reflect variations in density along the scaffold, where the higher the fluorescent signal, the lower the local porosity, while maintaining a constant GelMA:DexMA gradient.

Following purification, printing fidelity and internal microstructural features were evaluated by means of micro–computed

tomography (Micro-CT). The results reported in Fig. 2e and f demonstrate the high spatial resolution achievable in the fabrication of 3D functionally graded hydrogel, confirming the ability of the mix-ff-MPH printing platform to accurately deposit porous FGMs in 3D. Micro-CT reconstructions revealed well-defined regions of interconnected pores interspersed with denser polymer domains, in agreement with the programmed modulation of porosity during printing. In the two-layer reference construct (30–70% porosity, Fig. 2e), a sharp transition between layers with distinct pore morphologies was clearly observed, as further supported by the corresponding pore size distribution analysis. In contrast, scaffolds featuring a continuous porosity gradient from 30% to 70% (Fig. 2f) exhibited a gradual evolution of pore architecture along the printing direction, without abrupt interfaces. Notably, the printed constructs preserved the designed architectural features throughout the entire volume, highlighting the capability of the mix-ff-MPH system to precisely pattern 3D FGMs with controlled pore size and density distributions.

Of note, we also demonstrated that the designed printing head can be further expanded and effectively used in combination with a higher number of continuous phase inlets, thus enabling an even higher degree of freedom in spatial biomaterial design and patterning. As illustrated in Fig. 2g, the designed micromixer unit efficiently mixed three different continuous phase inks (in this case we load the biopolymer solutions respectively with blue, yellow, and red pigments) producing a smooth colour transition, independently of the complexity of the printed object and of the bioink extrusion order.

3.3. Cell viability on the heterogeneous scaffold

Following the assessment of the mixing efficiency of our MPH and the successful fabrication of constructs with continuous 3D compositional gradients, we investigated how the scaffold's biochemical and biomechanical properties influence cell behaviour. Prior to cell seeding, the printed scaffolds were purified to eliminate residual surfactant and dispersed phase, and subsequently sterilized under UV light, ensuring a suitable environment for biological evaluation. For this purpose, 3T3 fibroblasts were seeded onto 3D-printed hydrogels featuring a continuous material gradient—from 100% DexMA at the base to 100% GelMA at the top. These two biomaterial inks were selected as the derived hydrogels offer significant differences in cell adhesiveness and mechanical properties. GelMA was selected due to its well-established biocompatibility and biodegradability and the soft nature of its gels, making it a widely used material in tissue engineering.[29] In contrast, DexMA hydrogels—while cytocompatible—are generally stiff and lack intrinsic adhesive moieties thus being naturally non-cell-adhesive.[30]

Live/dead assays confirmed high cell viability (>80%) throughout the gradient scaffold (Fig. 3a). Notably, a distinct transition in cell behaviour was observed approximately one-third up the scaffold height, marked by a yellow line in the sample cross-sections (Fig. 3a). This shift likely corresponds to the increasing presence of Arg-Gly-Asp (RGD) peptide motifs, naturally present in GelMA, which promote enhanced cell adhesion and interaction.[29] It is reasonable to assume that, as the proportion and concentration of GelMA increased along the gradient, a corresponding rise in fibroblast adhesion occurred, as shown in Fig. 3b. On the other hand, cells in the DexMA-rich region exhibited a markedly different morphology: instead of spreading on the surface, they tended to migrate into scaffold pores and form cellular aggregates. This behaviour contrasts with the more uniformly spread cells found in GelMA-dominant zones. A single graded architecture thus enabled the simultaneous assessment of cell responses across a continuous stiffness and biochemical spectrum. These findings are of the

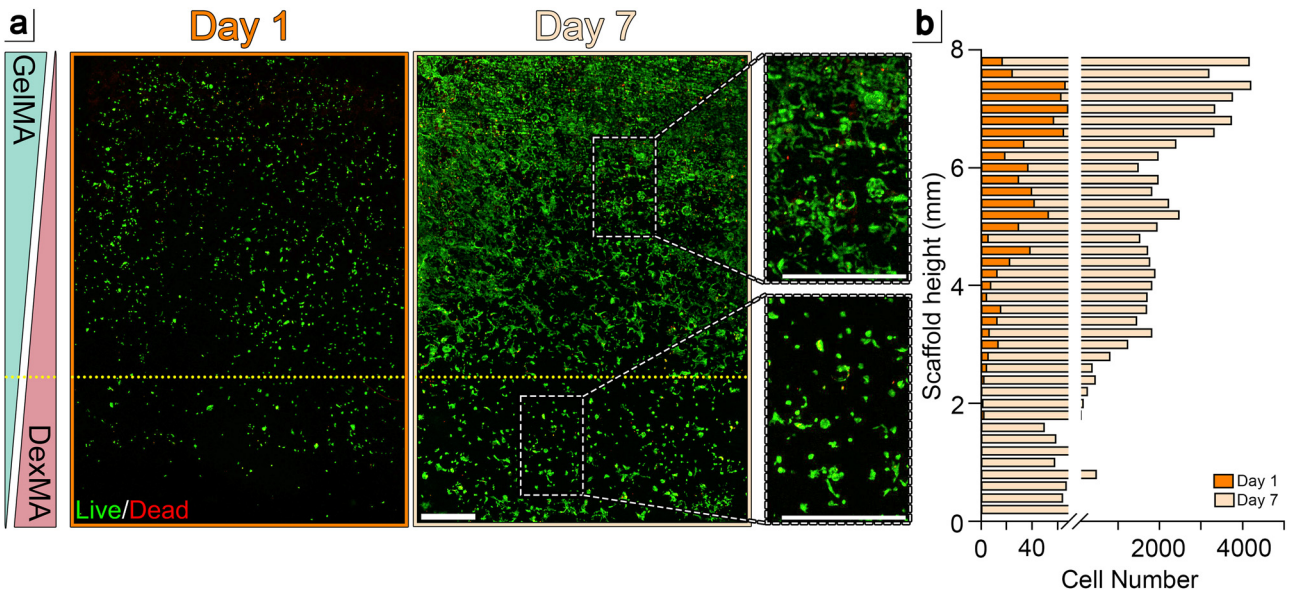

Fig. 3 3T3 fibroblast adhesion on a functionally graded hydrogel, 30% porosity - (a) live/dead staining of gradient sample DexMA (bottom) to GelMA (top). Day 1 and day 7. (b) Cell number counting along the gradient samples day 1 and day 7. Scale bar (a) 1 mm.

utmost importance for *in vitro* tissue modelling: in fact, one can leverage such features to rapidly screen cell-matrix interactions and overall cell behaviour across a large range of experimental conditions, thus identifying the most suitable microenvironments while minimizing experimental efforts and resources.

This transition was further investigated by fabricating homogeneous scaffolds made of either a single biomaterial (GelMA or DexMA) or a blend formulation with defined ratios of the two components (DexMA : GelMA = 100 : 0, 80 : 20, 50 : 50, 40 : 60, 0 : 100). Compression tests (Fig. 4a) on homogeneous scaffolds reveled a marked difference in Young's modulus, with the 80 : 20 sample having 2.5 fold higher (~400 kPa) modulus than 60 : 40 formulation. This result reflects the significant difference in mechanical properties among the various studied compositions: by decreasing DexMA content, the Young's modulus rapidly decreases resulting in increasingly softer hydrogel matrices. This trend is consistently reflected in subsequent cell behavior observed in the experiments. It is well known, in fact, that substrate stiffness is a crucial regulator of cellular processes such as adhesion, spreading, migration, and cytoskeletal remodeling.[29]

Specifically, as presented in the graph in Fig. 4b, fibroblast adhesion to the 100% DexMA sample was drastically low, almost absent, as further indicated in Fig. 4c by the low cell density and predominantly round morphology. Cells exhibited minimal interaction with the DexMA scaffold surface, lacking visible F-actin elongation or cytoskeletal organization, suggesting severely impaired attachment and spreading. Conversely, fibroblasts exhibited progressive growth and colonization of the scaffold, closely following the increasing GelMA proportion. In the 80 : 20 DexMA : GelMA sample, cell distribution appeared heterogeneous, with regions of high colonization interspersed with areas containing fewer cells. This trend became more pronounced starting from 60 : 40 scaffold, with increasing GelMA concentrations, culminating in the 100% GelMA scaffold, which was entirely covered and densely colonized by cells. Consequently, Col I expression (Fig. 4d) was observed only in regions where high cell density was present.

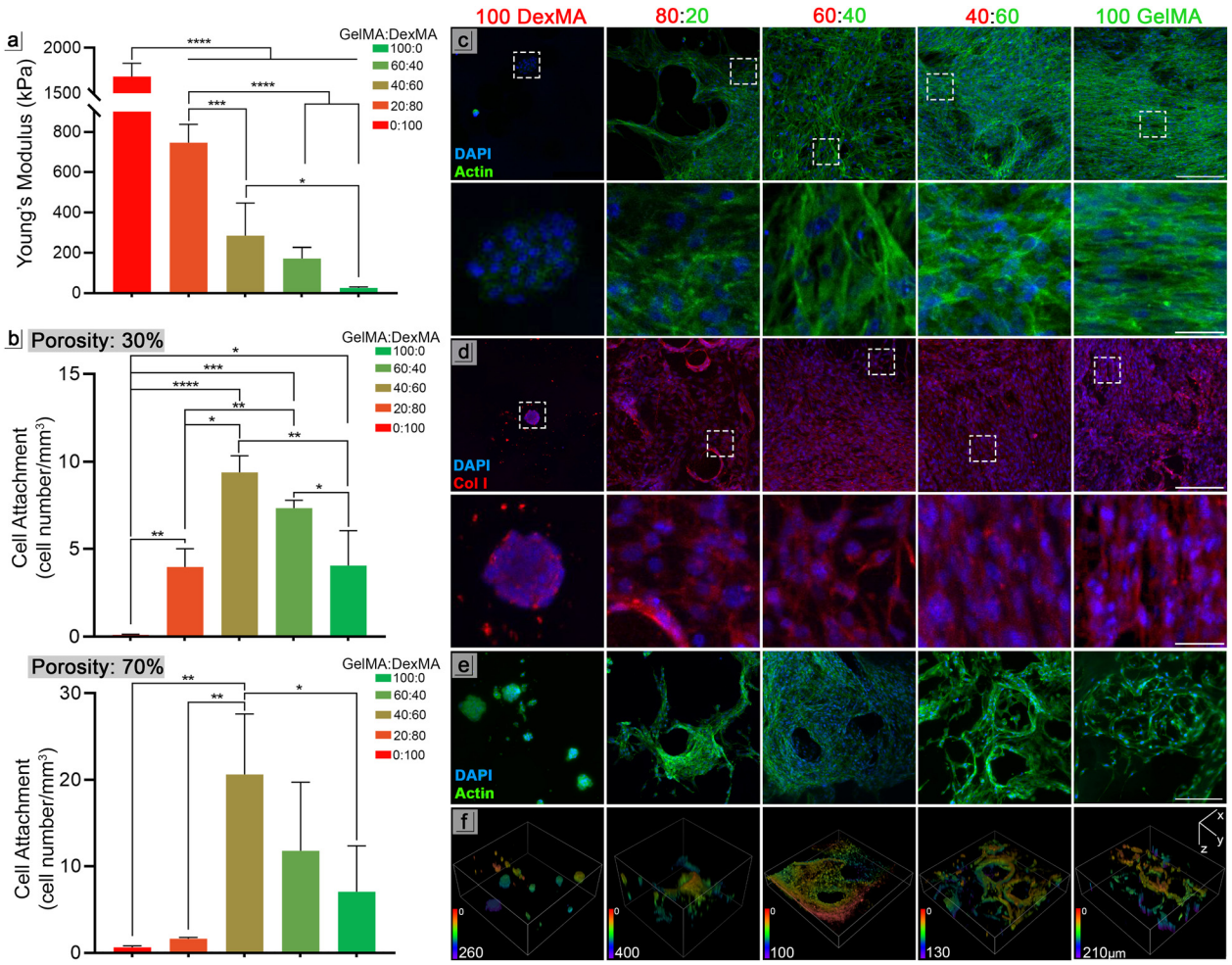

Fig. 4 3T3-fibroblast cell adherence study on GelMA:DexMA scaffold - (a) morphological characterization of 3D printed porous FGHs: variation of Young's moduli in samples characterized by DexMA – GelMA single and bi-composition. (b) Cell attachment analysis on scaffolds on day 7. Confocal laser microscopy images: (c) Actin (green) and DAPI (blue) staining of 3T3-fibroblast on different scaffolds (30% porosity) on day 7. (d) Collagen type I (red) and DAPI (blue) staining of 3T3-fibroblasts on different scaffolds (30% porosity) on day 7. (e) The line shows Actin (green) and DAPI (blue) staining of 3T3-fibroblast on different scaffolds (70% porosity) on day 7. (f) Z-stack imaging showing the depth-wise distribution of cells within the 3D scaffold. Scale bars (c) and (d) 200 µm and 40 µm, (e) 200 µm.

Cells exhibited an increased cytoskeletal remodelling as indicated by the abundant and well-organized actin filaments forming stress fibers, which are essential for cell spreading and mechanotransduction (Fig. 4c–e). These results suggest that a critical threshold in mechanical and biochemical properties governs the switch in cellular behavior. To further explore the effect of scaffold architecture over 3D cell organization, we fabricated scaffolds with up to 70% porosity and pore sizes of ~300 μm. In these highly porous constructs, we observed substantial cell migration throughout the scaffold volume, indicating effective three-dimensional colonization (Fig. 4e and f). A comparable cell distribution was noted in scaffolds with 30% porosity, although with more limited 3D penetration due to the limited pore interconnectivity.

Furthermore, the characterization of the GelMA-DexMA gradient introduces a dynamic aspect to the analysis. These observations emphasize the importance of identifying a proper tradeoff between the spatial organization and connectivity of the porous network to support proper three-dimensional cell colonization and cell interactions. While the 3T3 cell line represents a suitable cell model for preliminary validation of the fabricated pFGHs, we envisioned that the proposed microfluidic-assisted 3D printing platform may be effectively used to study cellular behavior in more relevant settings such as co-culture microenvironment mimicking tissue-interface models.

4. Conclusions

This study presented the successful design and implementation of a novel microfluidic printing head incorporating a passive micromixer (mix-ff-MPH) for 3D printing porous functional graded hydrogels (pFGHs) with tunable chemical composition and porosity. By integrating the micromixer upstream of the flow-focusing junction, we achieved precise, dynamic control over the mixing and patterning of biomaterial inks—enabling the fabrication of complex, spatially graded constructs.

The geometry of the micromixer was optimized to ensure efficient mixing, with the selected configuration achieving a mixing index (MI) $\geq$ 0.8, as verified by confocal microscopy. The mix-ff-MPH permitted on-demand modulation of the oil-in-water (O/W) emulsion ink composition by simply adjusting the volumetric ratio of continuous phase components. This, in turn, allowed for fine-tuned control over scaffold porosity. The seamless integration of the micromixer with the 3D printing platform enabled the fabrication of scaffolds with spatially defined variations in both porosity and chemical composition—critical attributes for engineering physiologically relevant tissue structures.

Preliminary cell tests with 3T3 fibroblasts conducted on the printed scaffolds revealed the significant impact of matrix composition on cellular behavior. Regions enriched with GelMA supported enhanced fibroblast attachment and proliferation, while those with higher DexMA content—owing to its inert character—exhibited reduced cell adhesion. These results demonstrate the capacity of graded scaffolds (i) to rapidly screen a spectrum of experimental conditions within a single sample and (ii) to elicit localized cellular responses, emphasizing the role of microenvironmental cues in regulating cell function.

Overall, the mix-ff-MPH offers a powerful and flexible tool for future biofabrication studies, where complex, multi-material architectures may be assembled with on-the-fly control over spatial composition and structure. Future work could explore the application of this system in co-culturing different cell types – including stem cells – or incorporating bioactive molecules to further tailor the cellular 3D microenvironment.

Extending this platform into perfused dynamic culture systems or toward cell-laden foam-based fabrication strategies to enable homogeneous cell distribution and sustained viability in larger volumes represents an important direction for future work. In this context, the proposed platform also provides a foundation for future studies exploring the combined effects of curvature, architecture, and material gradients on cell behavior.

Author contributions

Maria Celeste Tirelli: writing – original draft, visualization, validation, methodology, investigation, formal analysis, funding acquisition. Francesco Nalin, Nehar Celikkin: writing – review and editing, methodology, investigation. Żaneta Górecka, Pasquale Posabella: methodology, investigation. Wojciech Święszkowski: resources, funding acquisition. Marco Costantini: conceptualization, writing – review and editing, supervision, visualization, methodology, project administration, funding acquisition.

Conflicts of interest

There are no conflicts to declare.

Data availability

The datasets supporting the findings of this study have been deposited in the RepOD repository under the title "Microfluidic-Mixer Assisted 3D Printing of Functionally Graded Multimaterial Hydrogels for Engineering Complex Tissue Interfaces", DOI: 10.18150/X8EYX3, available at: https://doi.org/10.18150/X8EYX3.

Supplementary information (SI) is available. See DOI: https://doi.org/10.1039/d5ma01130b.

Acknowledgements

This article was funded by National Science Centre Poland (NCN) within OPUS 19 project no. 2020/37/B/ST8/02167 to M. C. and W. Ś. This research was also partially funded by National Science Centre Poland (NCN) within PRELUDIUM 23 project no. 2024/53/N/ST5/02609 to M. C. T.

Notes and references

1 A. Seidi, M. Ramalingam, I. Elloumi-Hannachi, S. Ostrovidov and A. Khademhosseini, Gradient biomaterials for soft-to-hard interface tissue engineering, *Acta Biomater.*, 2011, 7(4), 1441–1451, DOI: 10.1016/j.actbio.2011.01.011.

2 N. Yildirim, A. Amanzhanova, G. Kulzhanova, F. Mukasheva and C. Erisken, Osteochondral Interface: Regenerative Engineering and Challenges, *ACS Biomater. Sci. Eng.*, 2023, **9**(3), 1205–1223, DOI: 10.1021/acsbiomaterials.2c01321.
3 G. K. Jalandhra and K. A. Kilian, Biofabrication approaches to fabricating gradients and interfaces in osteochondral tissue engineering, *Curr. Opin. Biomed. Eng.*, 2024, **31**, 100544, DOI: 10.1016/j.cobme.2024.100544.
4 M. Sartori, *et al.*, A new bi-layered scaffold for osteochondral tissue regeneration: In vitro and in vivo preclinical investigations, *Mater. Sci. Eng., C*, 2017, **70**, 101–111, DOI: 10.1016/j.msec.2016.08.027.
5 J. Liu, L. Li, H. Suo, M. Yan, J. Yin and J. Fu, 3D printing of biomimetic multi-layered GelMA/nHA scaffold for osteochondral defect repair, *Mater. Des.*, 2019, **171**, 107708, DOI: 10.1016/j.matdes.2019.107708.
6 Y. Li, *et al.*, A Review on Functionally Graded Materials and Structures via Additive Manufacturing: From Multi-Scale Design to Versatile Functional Properties, *Adv. Mater. Technol.*, 2020, **5**(6), 1900981, DOI: 10.1002/admt.201900981.
7 T. J. Levingstone, E. Thompson, A. Matsiko, A. Schepens, J. P. Gleeson and F. J. O'Brien, Multi-layered collagen-based scaffolds for osteochondral defect repair in rabbits, *Acta Biomater.*, 2016, **32**, 149–160, DOI: 10.1016/j.actbio.2015.12.034.
8 A. Prasad, M. R. Sankar and V. Katiyar, State of Art on Solvent Casting Particulate Leaching Method for Orthopedic ScaffoldsFabrication, *Mater. Today Proc.*, 2017, **4**(2), 898–907, DOI: 10.1016/j.matpr.2017.01.101.
9 S. Wang, S. Zhao, J. Yu, Z. Gu and Y. Zhang, Advances in Translational 3D Printing for Cartilage, Bone, and Osteochondral Tissue Engineering, *Small*, 2022, **18**(36), 2201869, DOI: 10.1002/smll.202201869.
10 M. Marcotulli, *et al.*, Microfluidic 3D Printing of Emulsion Ink for Engineering Porous Functionally Graded Materials, *Adv. Mater. Technol.*, 2023, **8**(5), 2201244, DOI: 10.1002/admt.202201244.
11 F. Nalin, M. C. Tirelli, P. Garstecki, W. Postek and M. Costantini, Tuna-step: tunable parallelized step emulsification for the generation of droplets with dynamic volume control to 3D print functionally graded porous materials, *Lab Chip*, 2024, **24**(1), 113–126, DOI: 10.1039/D3LC00658A.
12 Q. Dai, *et al.*, Microfluidic bubble-templating 3D printing of ordered macroporous hydrogels, *Compos. Part B Eng*, 2024, **284**, 111725, DOI: 10.1016/j.compositesb.2024.111725.
13 F. Serpe, F. Nalin, M. C. Tirelli, P. Posabella, N. Celikkin, J. Jaroszewicz, W. Swieszkowski, A. Barbetta, E. Senturk, C. M. Casciola and G. Ruocco, Microfluidic 3D bioprinting of foamed fibers with controlled micromorphology, *ACS Appl. Mater. Interfaces*, 2025, **17**(9), 13632–13645, DOI: 10.1021/acsami.4c22450.
14 Z. Lamberger, S. Zainuddin, T. Scheibel and G. Lang, Polymeric Janus Fibers, *ChemPlusChem*, 2023, **88**(2), e202200371, DOI: 10.1002/cplu.202200371.
15 G. Cai, L. Xue, H. Zhang and J. Lin, A Review on Micromixers, *Micromachines*, 2017, **8**(9), 274, DOI: 10.3390/mi8090274.
16 I. H. Oevreeide, A. Zoellner, M. M. Mielnik and B. T. Stokke, Curved passive mixing structures: a robust design to obtain efficient mixing and mass transfer in microfluidic channels, *J. Micromech. Microeng.*, 2021, **31**(1), 015006, DOI: 10.1088/1361-6439/abc820.
17 X. Wang, Z. Liu, B. Wang, Y. Cai and Q. Song, An overview on state-of-art of micromixer designs, characteristics and applications, *Anal. Chim. Acta*, 2023, **1279**, 341685, DOI: 10.1016/j.aca.2023.341685.
18 'J Biomedical Materials Res - 2024 - Nedrelow - Osteochondral Regeneration With Anatomical Scaffold 3D-Printing Design.pdf'.
19 D. Han and H. Lee, Recent advances in multi-material additive manufacturing: methods and applications, *Curr. Opin. Chem. Eng.*, 2020, **28**, 158–166, DOI: 10.1016/j.coche.2020.03.004.
20 J. J. Senior, M. E. Cooke, L. M. Grover and A. M. Smith, Fabrication of Complex Hydrogel Structures Using Suspended Layer Additive Manufacturing (SLAM, *Adv. Funct. Mater.*, 2019, **29**(49), 1904845, DOI: 10.1002/adfm.201904845.
21 M. Costantini, *et al.*, Microfluidic Foaming: A Powerful Tool for Tailoring the Morphological and Permeability Properties of *Sponge-like* Biopolymeric Scaffolds, *ACS Appl. Mater. Interfaces*, 2015, **7**(42), 23660–23671, DOI: 10.1021/acsami.5b08221.
22 P. Jankowski, D. Ogończyk, L. Derzsi, W. Lisowski and P. Garstecki, Hydrophilic polycarbonate chips for generation of oil-in-water (O/W) and water-in-oil-in-water (W/O/W) emulsions, *Microfluid. Nanofluidics*, 2013, **14**(5), 767–774, DOI: 10.1007/s10404-012-1090-8.
23 C. Colosi, *et al.*, Microfluidic Bioprinting of Heterogeneous 3D Tissue Constructs Using Low-Viscosity Bioink, *Adv. Mater.*, 2016, **28**(4), 677–684, DOI: 10.1002/adma.201503310.
24 X. Feng, *et al.*, Tri-fluid mixing in a microchannel for nanoparticle synthesis, *Lab Chip*, 2019, **19**(17), 2936–2946, DOI: 10.1039/C9LC00425D.
25 H. S. Santana, D. S. Tortola, J. L. Silva and O. P. Taranto, Biodiesel synthesis in micromixer with static elements, *Energy Convers. Manag.*, 2017, **141**, 28–39, DOI: 10.1016/j.enconman.2016.03.089.
26 A. T. Young, O. C. White and M. A. Daniele, Rheological Properties of Coordinated Physical Gelation and Chemical Crosslinking in Gelatin Methacryloyl (GelMA) Hydrogels, *Macromol. Biosci.*, 2020, **20**(12), 2000183, DOI: 10.1002/mabi.202000183.
27 J. Idaszek, *et al.*, 3D bioprinting of hydrogel constructs with cell and material gradients for the regeneration of full-thickness chondral defect using a microfluidic printing head, *Biofabrication*, 2019, **11**(4), 044101, DOI: 10.1088/1758-5090/ab2622.
28 W. Raza, S. Hossain and K.-Y. Kim, A Review of Passive Micromixers with a Comparative Analysis, *Micromachines*, 2020, **11**(5), 455, DOI: 10.3390/mi11050455.
29 K. Yue, G. Trujillo-de Santiago, M. M. Alvarez, A. Tamayol, N. Annabi and A. Khademhosseini, Synthesis, properties, and biomedical applications of gelatin methacryloyl (GelMA) hydrogels, *Biomaterials*, 2015, **73**, 254–271, DOI: 10.1016/j.biomaterials.2015.08.045.
30 G. Trapani, M. S. Weiß and B. Trappmann, Tunable Synthetic Hydrogels to Study Angiogenic Sprouting, *Curr. Protoc.*, 2023, **3**(8), e859, DOI: 10.1002/cpz1.859.